JOURNAL OF Applied Polymer SCIENCE

Mechanical Modeling of a Three-Phase Nanocomposite Polymeric Material

Qingkai Meng, Daniel De Kee
Department of Chemical and Biomolecular Engineering and Tulane Institute for Macromolecular Engineering and Science, Tulane University, New Orleans, Louisiana 70118
Correspondence to: D. De Kee (E-mail: ddekee@tulane.edu)

ABSTRACT: The presented model to predict the elastic modulus of a polymer/ellipsoidal filler/oblate platelet system is based on Eshelby's equivalent inclusion method and Mori-Tanaka's back-stress analysis. We considered wood flour and intercalated clay particles in three-phase polymer nanocomposites as ellipsoidal and oblate platelet shapes, respectively. The intercalated clay particles along with the polymer chains in the clay galleries are treated as equivalent oblate fillers (EOFs). Via controlling wood flour and EOF aspect ratios (α and β) and the silicate layer number (n) in an EOF, the model prediction was compared with experimental data. The model predicted α and β values are within a range of 2.4–5 and 44–75, respectively, which are in good agreement with experimental observations. Quantitative agreement between model prediction and experimental data is achieved for $\alpha = 3.7$ and $\beta = 75$ when $n = 2$. The proposed model recovers the two-phase results for polymer/ellipsoidal filler systems or polymer/oblate platelet systems. © 2012 Wiley Periodicals, Inc. J. Appl. Polym. Sci. 000: 000–000, 2012

KEYWORDS: polymer nanocomposites; nanoclay; wood flour; modeling; micromechanics

Received 4 August 2010; accepted 10 May 2012; published online
DOI: 10.1002/app.38049

INTRODUCTION

Composite materials have been intensively studied in the recent past because of their improved and novel properties compared to the component materials.[1–7] Among these composite materials, polymer-based composites attract substantial academic and industrial attention, as such materials are extensively used. New polymeric matrices, reinforcement fillers, and compounding formulations are of substantial interest, as is the development of models to direct the design and preparation of composite materials. Several theories were considered to predict the mechanical, thermal expansion, and other properties in terms of the elastic properties of the matrix and filler, the geometry of the filler particles, and the overall morphology of the composite. Here, we focus on micromechanics methods, which are shown to be useful for characterizing polymer-based composite materials.

These micromechanics methods, including the dilute Eshelby, Mori-Tanaka, self-consistent, bounding, Halpin-Tsai, and shear lag models, are used to characterize the mechanical and thermal properties of two-phase polymer-based composites.[8] A wide range of filler materials have been used to reinforce polymeric matrices, but for a specific type of composite, only one type of filler, such as wood fiber, clay, carbon nanotubes, or glass fibers, was used. These filler particles are always considered to be spherical, cylindrical, or disc shaped. In some cases, such as for nanocomposites based on partially exfoliated and intercalated aluminosilicate platelets from montmorillonite-based organoclays, three-phase conditions should be considered. Luo and Daniel developed a three-phase model based on the Mori-Tanaka method to calculate the moduli of nanocomposites consisting of an epoxy matrix, exfoliated clay platelets, and intercalated clay clusters, as a function of various parameters, such as clay concentration, exfoliation ratio, exfoliated clay layer aspect ratio, intercalated clay cluster aspect ratio, layer spacing, and intragallery stiffness factors.[9] With the appropriate parameters obtained from the experiment, the prediction of the three-phase model is in good agreement with the measured results. Taya and Chou also developed a three-phase model via a combination of Eshelby's equivalent inclusion method and Mori-Tanaka's back stress analysis.[10,11] Two fillers (inhomogeneities) were considered as ellipsoidal and spherical shapes to take advantage of the calculation method introduced by Eshelby. In our study, a new three-phase composite was prepared by reinforcing polylactide (PLA) with wood flour and clay particles concurrently. It is interesting to note that in this three-phase system, wood flour and clay particles have different characteristic shapes and large size variations. To our knowledge, such a system has not yet been modeled via micromechanics methods to predict

mechanical properties. We extended Taya and Chou's method to our PLA-wood flour-clay particle system and compared the theoretical predictions with the experimental results.

Different characteristic shapes were emphasized, and we developed a theoretical analysis by considering wood flour particles as ellipsoidal fibers and intercalated clay particles as equivalent oblate platelet fillers. Our experimental results suggested that we consider the clay particles as intercalated clay clusters with a stack number n. The reinforcement fillers were characterized by two different aspect ratios, α for wood flour and β for the equivalent oblate platelet fillers.

THEORETICAL BASIS

To better understand the development of our model, we briefly recall Eshelby's method of equivalent inclusion. Eshelby developed a method to solve the elastic field in an elastic medium disturbed by an included subregion. "Eigenstrain" is a generic name that refers to nonelastic strains such as thermal expansion, phase transformation, and initial strains. In Eshelby's paper, eigenstrains refer to stress-free transformation strains in a region within an infinite homogeneous isotropic elastic medium.[12] A region within an elastic medium, which has the same elastic modulus as the remainder of the elastic medium, is called an inclusion. A region with different elastic modulus from that of the remainder is an inhomogeneity. Eigenstrain is associated with an inclusion or an inhomogeneity but is zero in the remainder of the elastic medium. An inclusion undergoing a change of shape and size disturbs the elastic state of the inclusion and matrix. A simple set of imaginary cutting, straining, and welding operations helps to determine what the elastic states of inclusion and matrix are. The inclusion is cut along the interface between the inclusion and the matrix and removed from the matrix. After removing, the inclusion experiences a stress-free transformation which is also called eigenstrain $\varepsilon^{\star}$. Surface tractions are chosen to restore the inclusion to its original form. The restored inclusion is returned/rejoined with the surrounding matrix. The surface tractions are replaced by body forces and the transformation causes a complicated strain distribution $\varepsilon^{C}(\boldsymbol{x})$ in the entire body. Eshelby shows that within an ellipsoidal inclusion the strain distribution $\varepsilon^{C}(\boldsymbol{x})$ is uniform and is related to the eigenstrain $\varepsilon^{\star}$ by

$$\varepsilon^{C} = \boldsymbol{S}\varepsilon^{*} \tag{1}$$

where $\boldsymbol{S}$ is Eshelby's tensor and depends on the inclusion geometry and the matrix elastic constant.

For a case of an infinite homogeneous isotropic elastic body containing ellipsoidal inhomogeneities, Eshelby postulated that the inhomogeneities can be simulated by inclusions in the homogeneous matrix with a fictitious eigenstrain $\varepsilon^{\star}$. Assuming that the entire body is subject to a uniform applied strain ε^{A} at infinity, one obtains via Eshelby's equivalent inclusion method

$$\boldsymbol{C}^{m}(\varepsilon^{A} + \varepsilon^{C} - \varepsilon^{*}) = \boldsymbol{C}^{I}(\varepsilon^{A} + \varepsilon^{C}) \tag{2}$$

where $\boldsymbol{C^m}$ and $\boldsymbol{C^I}$ are the elastic constant tensors for the matrix and the inhomogeneities, respectively, and ε^{C} is the complicated strain field introduced by the presence of the inhomogeneities. Via eqs. (1) and (2), one notes that the eigenstrain $\varepsilon^{\star}$ is proportional to the uniformly applied strain ε^{A}

$$\varepsilon^{*} = \frac{\boldsymbol{C}^{I} - \boldsymbol{C}^{m}}{[(\boldsymbol{C}^{m} - \boldsymbol{C}^{I})\boldsymbol{S} - \boldsymbol{C}^{m}]}\varepsilon^{A} \tag{3}$$

Mori and Tanaka provided a method of calculating the average internal stress in a matrix containing inclusions with transformation strain.[11] Their method shows that the average stress in the matrix is uniform throughout the material and the actual stress in the matrix is the average stress plus the locally fluctuating stress due to the inclusions. The average of the locally fluctuating stress vanishes in the matrix.

Taya and Chou developed a method to obtain the longitudinal Young's modulus of fiber-fiber and fiber-particulate systems based on Eshelby's equivalent inclusion theorem and Mori-Tanaka's bask stress analysis.[10] Taya and Chou's method simulates the conditions with high inhomogeneity volume fraction and the interaction between inhomogeneities. They assumed that the elastic body (matrix) is infinite and isotropic and that there is an infinite number of two kinds of inhomogeneities in the matrix. The matrix and inhomogeneities are linearly elastic and the inhomogeneities are either isotropic or transversely isotropic. All inhomogeneities are aligned in the uniaxial loading direction. The interfacial adhesion between the matrix and the inhomogeneities is perfect. We briefly review the Taya-Chou method and adapt it to our PLA/clay/wood nanocomposites.

An external stress σ^{0}_{ij} (see Figure 1, σ^{0}_{ii} refers to σ^{0}_{33}.) is applied to the composite. The polymer matrix acquires a disturbed stress field given by:

$$\langle \sigma_{ij} \rangle_{M} = C^{0}_{ijkl}\tilde{\varepsilon}_{kl} \tag{4}$$

where $\tilde{\varepsilon}_{kl}$ is the average strain disturbance due to all Ω_1 and Ω_2. The $< >$ bracket refers to the volume average value. C^{0}_{ijkl} is the elastic constant of the matrix, correspondingly, C^{1}_{ijkl} and C^{2}_{ijkl} are the elastic constants for Ω_1 and Ω_2, respectively. Single inhomogeneities Ω_1 and Ω_2 are introduced into the nanocomposite successively. From this two-step introduction, we obtain two fundamental equations over the entire composite domain (D), via Eshelby's equivalent inclusion method.

$$\sigma^{0}_{ij} + \sigma^{1}_{ij} = C^{0}_{ijkl}(\varepsilon^{0}_{kl} + \tilde{\varepsilon}_{kl} + \varepsilon^{1}_{kl} - \varepsilon^{*}_{kl}) = C^{1}_{ijkl}\left(\varepsilon^{0}_{kl} + \tilde{\varepsilon}_{kl} + \varepsilon^{1}_{kl}\right) \tag{5a}$$

$$\sigma^{0}_{ij} + \sigma^{2}_{ij} = C^{0}_{ijkl}\left(\varepsilon^{0}_{kl} + \tilde{\varepsilon}_{kl} + \varepsilon^{2}_{kl} - \varepsilon^{**}_{kl}\right) = C^{2}_{ijkl}\left(\varepsilon^{0}_{kl} + \tilde{\varepsilon}_{kl} + \varepsilon^{2}_{kl}\right) \tag{5b}$$

σ^{1}_{ij}, σ^{2}_{ij}, ε^{1}_{ij}, ε^{2}_{ij} are the disturbances of the stress and strain due to these single inhomogeneities, respectively. ε^{*}_{ij} and ε^{**}_{ij} are the eigenstrains, which are used to simulate the inhomogeneities, corresponding to Ω_1 and Ω_2, respectively. Note that for the entire composite domain D, $\sigma^{0}_{ij} = C^{0}_{ijkl}\varepsilon^{0}_{kl}$ always holds.

Eshelby's calculations yield:

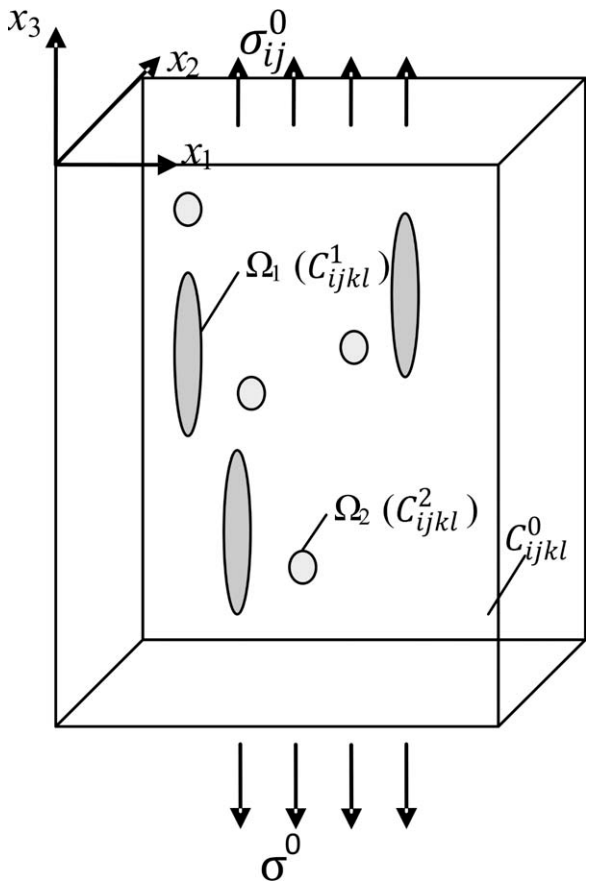

Figure 1. Sketch of a composite system. Ω_1 and Ω_2 denote the fiber and oblate platelet inhomogeneities. C_{ijkl}^0, C_{ijkl}^1, and C_{ijkl}^2 represent the elastic constants of the matrix, Ω_1 and Ω_2, respectively.

$$\varepsilon_{kl}^1 = S_{klmn}^1 \varepsilon_{mn}^* \qquad \text{in } \Omega_1 \tag{6.a}$$

$$\varepsilon_{kl}^2 = S_{klmn}^2 \varepsilon_{mm}^{**} \qquad \text{in } \Omega_2 \tag{6.b}$$

where S_{klmn}^1 and S_{klmn}^2 are the Eshelby tensors for Ω_1 and Ω_2, respectively. The Eshelby tensors depend only on C_{ijkl}^0 and on their respective specific geometries.

One can eliminate ε_{kl}^1 and ε_{kl}^2 in eqs. (5) via the relations in eqs. (6). Hence, we have three unknown variables $\tilde{\varepsilon}_{ij}$, ε_{ij}^*, and ε_{ij}^{**} which can be solved via eqs. (5) and the equilibrium condition $\int_D \sigma_{ij} dV = 0$, where σ_{ij} denotes the disturbed stresses including $\langle \sigma_{ij} \rangle_M$, σ_{ij}^1, and σ_{ij}^2. From the equilibrium condition, the relation between these three disturbed stresses is:

$$(1 - f_1 - f_2)\langle \sigma_{ij} \rangle_M + f_1 \left\langle \sigma_{ij}^1 \right\rangle + f_2 \left\langle \sigma_{ij}^2 \right\rangle = 0 \tag{7}$$

where f_1 and f_2 are the volume fractions of Ω_1 and Ω_2, respectively. Once $\tilde{\varepsilon}_{ij}$, ε_{ij}^* and ε_{ij}^{**} are determined, we can compute the longitudinal modulus of the nanocomposites by using the equivalence of the elastic strain energies,

$$\frac{(\sigma_{33}^0)^2}{2E_L} = \frac{(\sigma_{33}^0)^2}{2E_0} + \frac{\sigma_{33}^0 \varepsilon_{33}^* f_1}{2} + \frac{\sigma_{33}^0 \varepsilon_{33}^{**} f_2}{2} \tag{8}$$

To finally obtain the formula for the longitudinal modulus E_L as

$$\frac{E_L}{E_0} = \frac{1}{1+\eta} \tag{9}$$

where

$$\eta = f_1 \left\{ \frac{(B_3^* S_1 + B_4^* S_2)}{A^* S} + \frac{(B_4^* - v_0 B_3^*)}{A^*} \right\} + f_2 \left\{ \frac{(B_3^{**} S_1 + B_4^{**} S_2)}{A^{**} S} + \frac{(B_4^{**} - v_0 B_3^{**})}{A^{**}} \right\} \tag{10}$$

The expressions for A^*, A^{**}, and B_1^* are given in the appendix.

MODEL DEVELOPMENT

Considering wood flour and intercalated clay particles as two types of ellipsoidal inhomogeneities—elliptic fibers and oblate platelets as shown in Figure 2, we developed a model based on the method of Taya and Chou. In addition to the assumptions made by Taya-Chou, we also consider the following[13]:

- Wood flour particles are treated as elliptic fibers ($a_1 = a_2 < a_3$); clay particles (intercalated silicate layer clusters) are treated as oblate platelets ($a_1 < a_2 = a_3$). All clay particles are considered intercalated, forming clay clusters with parallel stacked n single silicate layers.
- Wood flour particles are aligned uniaxially along the loading axis x_3 as shown in Figure 2, clay platelets are aligned in such a way that the biaxial surface is parallel to the x_3 axis, and the direction normal to the biaxial surface is random. All inhomogeneities are distributed uniformly in the matrix except for the direction normal to the biaxial surfaces of the clay platelets.

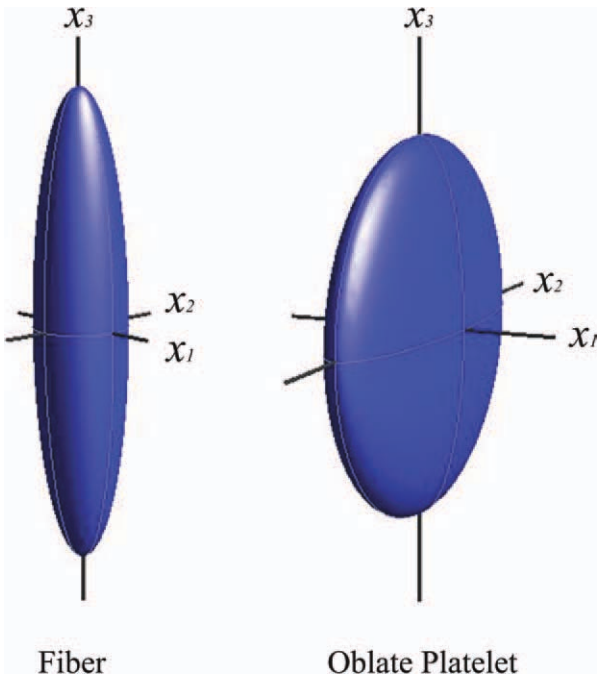

Figure 2. Physical representations, coordinate systems used for the calculation of composite stiffness based on fiber and oblate plate reinforcement (fiber: $a_1 = a_2 < a_3$; oblate platelet: $a_1 < a_2 = a_3$; a_1, a_2, and a_3 are the radii along axes x_1, x_2, and x_3, respectively). [Color figure can be viewed in the online issue, which is available at wileyonlinelibrary.com.]

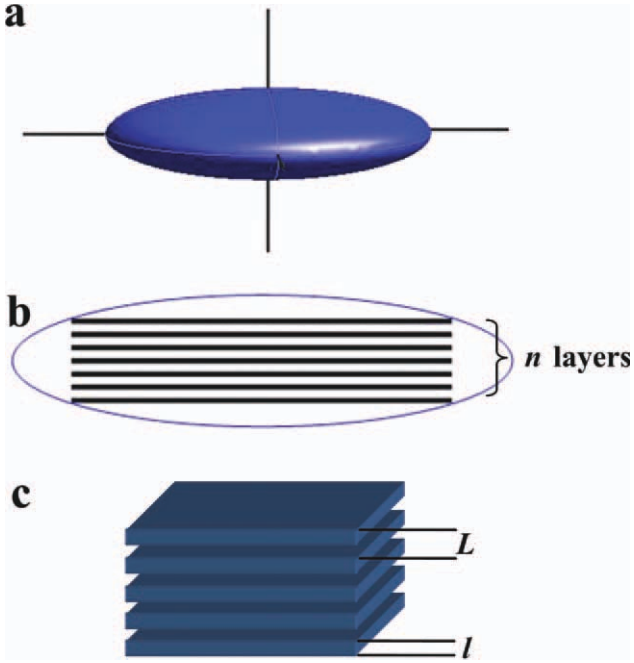

Figure 3. Intercalated clay silicate layer cluster (a) and its axial sectional view (b), each line in (b) represents one silicate layer. The intercalated clay "*d*-spacing" L and silicate layer thickness l are shown in (c). [Color figure can be viewed in the online issue, which is available at wileyonlinelibrary.com.]

TEM images confirm that the clay particles are mostly intercalated and partially exfoliated in the PLA matrix. The polymer matrix molecules and the silicate layers are of equivalent size, and the interactions of the silicate layers with the polymer matrix molecules around the nanofillers at nanometer length scale are more concentrated than for the bulk polymer molecules. The polymer matrix inside the nanofillers at nanometer scale cannot be treated as isotropic as for the bulk polymer molecules. We, therefore, consider the intercalated clay particles together with the polymer molecules in the galleries as equivalent oblate fillers (EOFs) as shown in Figure 3.

The longitudinal elastic constant (E_{EOF}) and biaxial direction Poisson ratio (v_{EOF}) for the lamellar silicate layers reinforced EOFs are determined via a nanoscale model for intercalated clusters as[9]:

$$E_{EOF} = V_f E_f + (1 - V_f) E_m + \frac{(v_f - v_m)^2}{\frac{1-v_f^2}{V_f E_f} + \frac{1-v_m^2}{(1-V_f)E_m}} \tag{11}$$

$$v_{EOF} = \left[V_f v_f + (1 - V_f) v_m - v_f v_m\right] \frac{V_f(1 + v_m)E_f + (1 - V_f)(1 + v_f)E_m}{V_f(1 - v_m^2)E_f + (1 - V_f)(1 - v_f^2)E_m} \tag{12}$$

where V_f is the volume fraction of inorganic silicate layers in an EOF; E_f and E_m are the elastic constants of the silicate layer and the polymer matrix, respectively; v_f and v_m are the Poisson ratios for the inorganic clay silicate layers and the polymer matrix, respectively.

Assuming that there are n silicate layers in an EOF and the geometry of a silicate layer is assumed to be a disk of thickness l and L is the d-spacing of intercalated clay as shown in Figure 3, we can determine V_f as:

$$V_f = \frac{nl}{(n-1)L + l} \tag{13}$$

V_f refers to the volume fraction of inorganic silicate layers in EOFs.

We calculate the Eshelby tensors for the intercalated clay clusters based on the oblate ellipsoid shape in the coordinate system and the alignment direction of clay clusters as shown in Figures 1 and 2 via the Mura method.[14] We obtain:

$$S^2_{1111} = S^2_{3333} = \frac{1}{4(1-v_0)}\left[\frac{3}{2} - \frac{3\beta^2(2+\beta^2)}{2(\beta^2-4)^2} - \frac{4-8v_0}{(\beta^2-4)}\right] + \frac{\beta^2 \cos^{-1}\left(\frac{2}{\beta}\right)}{16(1-v_0)(\beta^2/4-1)^{3/2}}\left[1 - 2v_0 + \frac{9\beta^2}{4(\beta^2-4)}\right] \tag{14a}$$

$$S^2_{1122} = S^2_{3322} = \frac{1}{(1-v_0)(\beta^2-4)}\left[3 - 2v_0 + \frac{12}{(\beta^2-4)}\right] - \frac{\beta^2 \cos^{-1}\left(\frac{2}{\beta}\right)}{16(1-v_0)(\beta^2/4-1)^{3/2}}\left[1 - 2v_0 + \frac{12}{(\beta^2-4)}\right] \tag{14b}$$

$$S^2_{1133} = S^2_{3311} = \frac{1}{4(1-v_0)}\left[\frac{1}{2} - \frac{\beta^2(2+\beta^2)}{2(\beta^2-4)^2} + \frac{4-8v_0}{(\beta^2-4)}\right] + \frac{\beta^2 \cos^{-1}\left(\frac{2}{\beta}\right)}{16(1-v_0)(\beta^2/4-1)^{3/2}}\left[-1 + 2v_0 + \frac{3\beta^2}{4(\beta^2-4)}\right] \tag{14c}$$

where β ($= a_3/a_1$) is the aspect ratio of the EOFs when $n > 1$ and the aspect ratio of single silicate layers when $n = 1$ and v_0 is the Poisson ratio of the matrix.

EXPERIMENTAL

The PLA used in this study was PLA 2002D purchased from NatureWorks. The density of the PLA is 1.24 g/cm^3. The layered silicate used in this study was Cloisite® 20A from Southern Clay Products Inc. The density of the clay is 1.77 g/cm^3 with a mean interlayer spacing of the (001) plane $d_{001} = 2.42$ nm. The organic content in Cloisite® 20A, reported by supplier, is 38 wt %. When calculating the silicate layer volume fraction, the organic modifiers in nanoclay were approximately treated as the same polymer as the matrix. The hardwood (maple) was obtained from ExxonMobil.

All PLA/clay/wood nanocomposite samples were prepared via twin-screw extrusion and injection molding, according to the method described in our previous paper.[15] The sample compositions are summarized in Table I.

The tensile tests were performed with an Instron 5582 materials testing machine. The tension tests were based on the ASTM D638 standard at a crosshead speed of 5 mm/min and at 23 ±

Table I. PLA/Clay/Wood Nanocomposite Sample Compositions

	Weight %			Volume %	
Sample	PLA	Wood flour	Cloisite® 20A	Wood flour	Silicate layer
P1C	99	0	1	0	0.27
P3C	97	0	3	0	0.82
P5C	95	0	5	0	1.38
P0C30W	70	30	0	50.8	0
P1C30W	69	30	1	51.0	0.19
P3C30W	67	30	3	51.4	0.58
P5C30W	65	30	5	51.8	0.97

1°C. A Siemens D500 X-ray diffractometer was used to measure the *d*-spacing of the nanoclay in the nanocomposites at room temperature. The X-ray beam was Cu-Kα ($\lambda = 0.154$ nm) radiation, operated at 43 KV and 38 mA. The scanning rate was 0.01°/s and the 2θ ranged from 1.06 to 30°. A Jeol 2010 transmission electron microscope (TEM) was used to examine the nanocomposite morphology at an acceleration voltage 200 KV. Wood flour particles were stuck directly on a piece of carbon tape and mounted on a SEM sample holder. The morphology and size of the wood flour particles were observed using a Jeol JSM-820 scanning electron microscope (SEM) at an acceleration voltage of 20 kV. The SEM samples were sputter-coated with gold before observation.

RESULTS AND DISCUSSION

Determination of Physical Constants

The values of the density (ρ), elastic modulus (E), and Poisson ratios (v) of the components (PLA, wood flour, and clay) were taken from literatures and from the technical data supplied by the manufacturers (see Table II). The Lamé constants (μ and λ) were calculated via the elastic modulus E and the Poisson ratio v as follows:

$$\lambda = 2\mu v/(1-2v) \tag{15}$$

$$E = 2(1+v)\mu \tag{16}$$

We determined that $l = 1$ nm and $L = 3.5$ nm via XRD and TEM data/images, therefore

$$V_f = \frac{nl}{(n-1)L+l} = \frac{2n}{7n-5} \tag{17}$$

Submitting eq. (17) and the E and v values of the neat PLA and the silicate layer into eqs. (11) and (12), we can obtain the longitudinal elastic constant (E_{EOF}) and biaxial direction Poisson ratio (v_{EOF}) for the EOFs as a function of silicate layer number n.

Model predictions were compared with experimental data (see Table III). The polymer clay nanocomposites (PCNs) and polymer clay wood nanocomposites (PCWNs) data were from our research, and the polymer wood composites (PWCs) data were obtained from the paper by Huda et al.[16]

Table II. Key Physical Properties of PLA, Wood Flour, and Clay

	E (GPa)	Poisson's ratio ν	μ (GPa)	λ (GPa)	density ρ (g/cm^3)
PLA	3.75	0.35	1.39	3.24	1.24
Wood	9.6	0.45	3.31	29.79	0.51
Clay[17]	178	0.20	74.17	49.44	2.83

Polymer-Ellipsoidal Filler System

Note that by setting $f_2 = 0$ in eq. (10), the model recovers the results for a polymer-ellipsoidal filler system, given by:

$$\frac{E_L}{E_0} = \frac{1}{1+f_1\left\{\frac{\left(B_3^* S_1 + B_4^* S_2\right)}{A^* S} + \frac{\left(B_4^* - v_0 B_3^*\right)}{A^*}\right\}} \tag{18}$$

The volume fraction f_2 in S, S_1, and S_2 (see Appendix) also vanishes and the three-phase composite model has been reduced to a two-phase model. We examine the effect of varying wood flour aspect ratio (α) on the elastic modulus of the composites and compare the predictions with those of three other models, the Voigt, Reuss, and Halpin-Tsai models. The Voigt, Reuss, and Halpin-Tsai models are given by:

$$E_L^{\text{Voigt}} = V_0 E_0 + V_1 E_1 \tag{19}$$

$$E_L^{\text{Reuss}} = \frac{1}{\frac{V_0}{E_0} + \frac{V_1}{E_1}} \tag{20}$$

$$\frac{E_L^{H-T}}{E_0} = \frac{1+\zeta\eta V_1}{1-\eta V_1} \tag{21}$$

where V_0 and E_0 refer to the matrix volume fraction and longitudinal elastic modulus; similarly V_1 and E_1 refer to the filler volume fraction and longitudinal elastic modulus. In the

Table III. Elastic Modulus Experimental Data for Neat PLA, PCNs, PCWNs, and PWCs

			Volume fraction %	
Sample	E_L (GPa)	E_L/E_O	Wood flour	Inorganic silicate layer
Pure PLA	3.75	1	0	0
P1C	4.10	1.17	0	0.27
P3C	4.25	1.22	0	0.82
P5C	4.56	1.30	0	1.38
P0C30W	5.87	1.68	50.8	0
P1C30W	6.28	1.79	51.0	0.19
P3C30W	6.65	1.90	51.4	0.58
P5C30W	7.09	2.03	51.8	0.97
Neat PLA[a]	2.7	1	0	0
P20W	4.8	1.78	37.6	0
P30W	5.3	1.96	50.8	0
P40W	6.3	2.33	61.7	0

[a]PLA matrix used by Huda et al.[16]

Applied Polymer SCIENCE

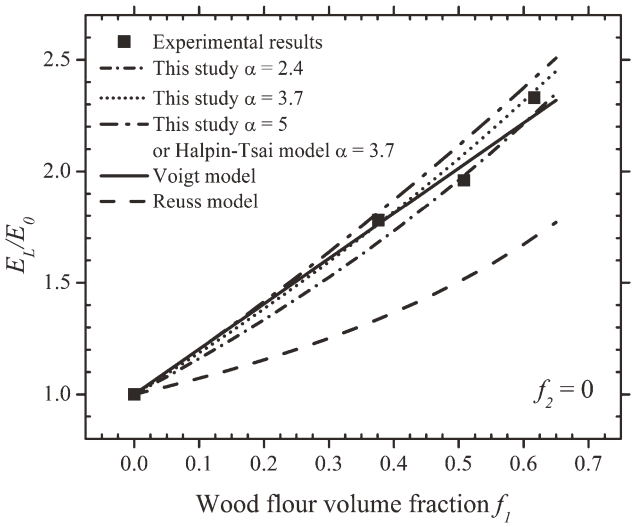

Figure 4. Comparison between experimental results and theoretical predictions [Eqs. (18–22)] for elastic modulus as a function of wood flour volume fraction f_1 with $f_2 = 0$ and various aspect ratios α.

Halpin-Tsai model, ζ is a parameter dependent upon the geometry and loading direction of filler, and η is given by

$$\eta = \frac{\frac{E_1}{E_0} - 1}{\frac{E_1}{E_0} + \zeta} \tag{22}$$

Here $\zeta = 2(a/b)$, which was determined by Ashton et al.[16] and also used by Fornes and Paul[18]; the symbols a and b represent the length and diameter for ellipsoidal fillers or the diameter and thickness for oblate platelet fillers.

The experimental results and model predictions for PLA/wood flour composites are compared in Figure 4. The wood flour particles we used in this study are shown in a SEM image inset in Figure 5 as well as the distribution of wood flour aspect ratio

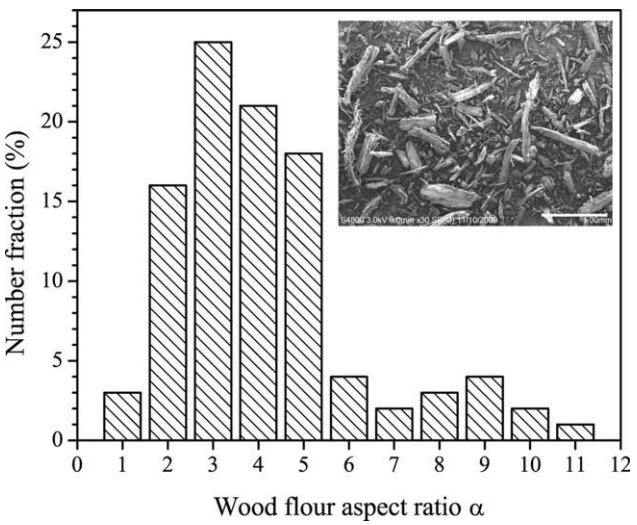

Figure 5. Aspect ratio distribution of wood flour calculated based on sufficient SEM images and an inset SEM image of wood flour particles (scale bar = 1 mm).

Figure 6. Transmission electron microscopy (TEM) image of PLA nanocomposite containing 3 wt % clay.

(α). The number average aspect ratio before extrusion was calculated based on sufficient numbers of SEM images. The wood flour particles exhibiting inconsistent geometry and size possess an average aspect ratio of 3.7 ± 1.3. Model predictions with three different aspect ratio values α = 2.4, 3.7, and 5 were also compared in Figure 4. Obviously, the elastic modulus is increasing with increasing wood flour volume fraction for both experimental results and model predictions. The model prediction for α = 2.4 shows a fair agreement with the experimental results considering the curve passes through the data point at $f_2 = 51$ vol %. The slope of predicted curves increases as the aspect ratio α increases from 2.4 to 5. The predicted curve of α = 3.7 from our proposed model properly fits the experimental results as passing through three data points. We should note that the increase in aspect ratio decreases the maximum random packing fraction according to Sudduth's work[19,20]; therefore, beyond certain wood flour volume fraction the elastic modulus will decrease with the volume fraction. For aspect ratio values from 2.4 to 5, the maximum random packing fraction was calculated to be from about 63 to 56 vol %. Because our composite materials were prepared by twin-screw extrusion generally generating high shear stress and we assume that wood flour particles are aligned uniaxially along loading axis in our model, our experimental data and model predictions do not show elastic modulus decrease with wood flour volume fraction. The predicted curve from our model with α = 5 almost overlaps the prediction from the Halpin-Tsai model with α = 3.7. To be clearly presented, only one predicted curve was plotted in the figure for the two cases. Compared to our proposed model, the Halpin-Tsai model tends to underestimate wood flour aspect ratio probably due to neglecting the effect of Poisson ratios of different component materials. Our proposed model with α = 2.4 and 5 creates an area bounded by the two predicted curves

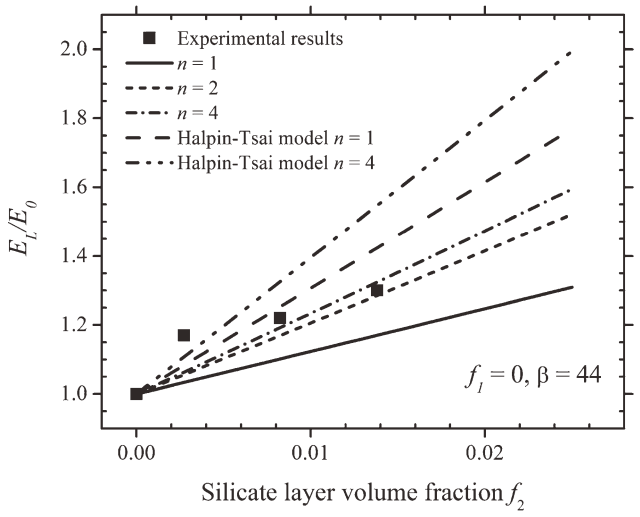

Figure 7. Effect of intercalated silicate layer number (n) in an equivalent oblate filler on the elastic modulus of nanocomposites with $f_1 = 0$ and $\beta = 44$ [Eqs. (11, 12, 17, 21–23)].

where the experimental results at various wood flour volume fractions are likely scattered. This is particularly true with considering the nonuniform particle size, random flour alignment, wood flour particle aggregation and poor interfacial adhesion in the composites[21] as well as possible aspect ratio reduction resulting from wood fiber damage during twin-screw extrusion.[22,23] The predicted curve by the Reuss model is much lower than the experimental results, and the prediction of the Voigt model is comparable to that of our model with $\alpha = 3.7$ except that at high wood flour volume fractions the Voigt model predicts lower values than our model does. To be noted that the Voigt and Reuss models do not take any filler shape parameters into account.

Polymer-Oblate Platelet System

By setting $f_1 = 0$, eq. (10) was reduced into a model for polymer-clay systems, given by:

$$\frac{E_L}{E_0} = \frac{1}{1 + f_2\left\{\frac{\left(B_3^{**}S_1 + B_4^{**}S_2\right)}{A^{**}S} + \frac{\left(B_4^{**} - v_0 B_3^{**}\right)}{A^{**}}\right\}} \quad (23)$$

An EOF aspect ratio β of 2 would introduce an infinity, as a denominator in eq. (14) involves $\beta^2 - 4$. The number of silicate layers in an EOF (n) was varied from 1 to 4 in this study.

Figure 6 illustrates the clay dispersive structures in a PLA nanocomposite containing 3 wt % clay. A microsize tactoid and intercalated and exfoliated silicate layers are observed in the TEM image. Based on the TEM observation and our earlier XRD analysis,[15] the clay particles in the nanocomposites are mostly in an intercalated structure and only few in an exfoliated structure. The n value of 1 refers to a fully exfoliated structure, which is obviously not applicable to our nanocomposites. The intercalated and partially exfoliated structures for our case were approximately treated as a solo intercalated structure, and there are n silicate layers in each clay cluster.

Figure 7 presents the effect of the number of intercalated layers in an EOF (n) on theoretical prediction at $f_1 = 0$ and $\beta = 44$. Note that when keep the aspect ratio of EOFs constant, larger n values should result in larger size particles in nanocomposites according to the model. The predicted curve obtained from our model for $n = 1$ is lower than the experimental results since for a fully exfoliated structure $\beta = 44$ is much lower than the real aspect ratio of single silicate layers. This confirms that an intercalated clay structure is dominant in the nanocomposites. The increase of the n value from 1 to 2 significantly increases the slope of predicted curve, meaning improved reinforcement effect of intercalated clay clusters than exfoliated silicate layers when they have a same aspect ratio ($\beta = 44$). Further increase of the n value from 2 to 4 continues increasing the curve slope but the slope increment is less than the previous one. In contrast to that the predictions from the Halpin-Tsai model for the same n values (1 and 4) are higher than the experimental results at 0.8 and 1.4 vol %, our model predictions are really getting

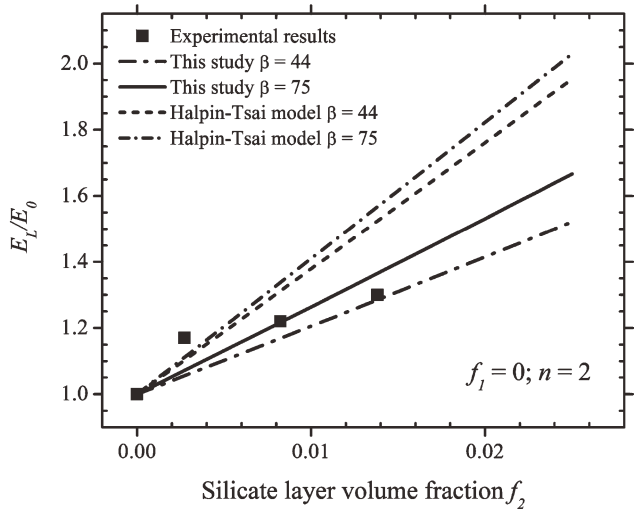

Figure 8. Effect of equivalent oblate filler aspect ratio (β) on the elastic modulus of nanocomposites with $f_1 = 0$ and $n = 2$ [Eq. (21–23)].

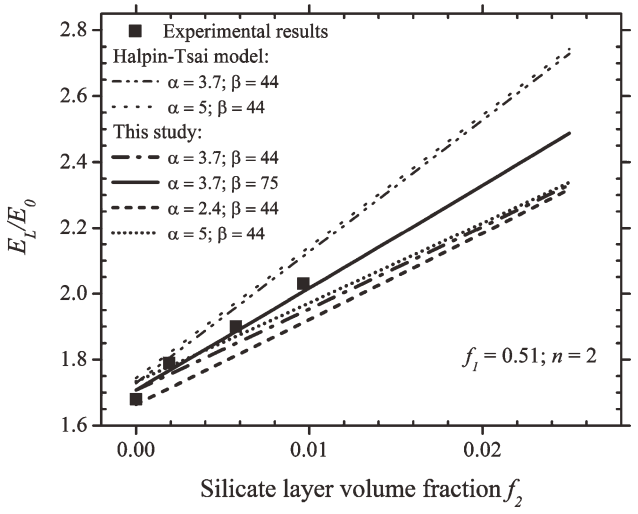

Figure 9. Experimental results and model predictions as a function of silicate layer volume fraction f_2 at $f_1 = 51\%$, $n = 2$ and various aspect ratios (α and β) [Eqs. (9 and 10)].

closed to these experimental results. As observed in the TEM image (Figure 6), the length of most clay particles is smaller than 500 nm; thus, we choose $n = 2$ for the following study.

Figure 8 presents the variation of elastic modulus as a function of silicate layer volume fraction predicted by our proposed model and the Halpin-Tsai model at $f_1 = 0$, $n = 2$ and two different aspect ratio ($\beta = 44$ or 75). According to Sudduth's model,[20] at a random packing fraction of 1.4 vol %, the aspect ratio β of clay in nanocomposites should be around 44. However, the morphology of silicate layers in the nanocomposites as observed by TEM in Figure 6 reveals that the silicate layers do align in a preferred direction as the flow direction during injection molding. Thus, it is possible that the aspect ratio β could be somewhat larger than 44. As shown in Figure 8, our model predictions for $\beta = 44$ and 75 pass through the experimental points at $f_2 = 1.4$ and 0.8 vol %, respectively; whereas, with the same aspect ratio values, the Halpin-Tsai model predicts larger values than our model does.

Polymer-Ellipsoidal-Oblate Platelet Filler Systems

Here, we consider the variation of elastic modulus as a function of silicate layer volume fraction at $f_1 = 51$ vol %, $n = 2$ and various aspect ratio pairs (α and β) (Figure 9). An aspect ratio pair $\alpha = 3.7$ and $\beta = 44$ was tested in both our proposed model and the Halpin-Tsai model, and both the theoretical predictions diverge from the experimental data as the silicate layer volume fraction increases. The proposed model predicts lower values with increasing silicate layer volume fraction; on the contrary, the Halpin-Tsai model leads to higher elastic modulus values. One observes quantitative agreement between the model prediction and the experimental data for $\alpha = 3.7$ and $\beta = 75$ for our proposed model. We could expect the increase in clay aspect ratio in the three-phase nanocomposites because the clay particles in the nanocomposites were twin-screw extruded twice according to the preparation procedure probably resulting in more silicate layer delamination. For a constant α value, increasing β value increases the slope of predicted curves, but they still share a same starting point at $f_2 = 0$; meanwhile, for a constant β value, increasing α value shifts entire curve to higher values. Note that the predicted curves with a same β value but different α values tend to converge as the silicate layer volume fraction increases, which is indicative of wood flour–silicate layer interaction. For the Halpin-Tsai model prediction in this case, we assume that the PLA/clay/wood nanocomposites form a two-phase system with the matrix properties being those of PLA/wood composite containing about 51 vol % wood flour. A second application of the Halpin-Tsai model predicts the elastic modulus of the three-phase system. The predicted curves from the Halpin-Tsai model are parallel to each other when they have a same β value but different α values and always higher than the predictions made by our proposed model at same aspect ratios. The Halpin-Tsai model can be used to predict elastic modulus of composites reinforced by one type of filler, such as clay or wood flour, with acceptable errors. However, for three-phase composite systems the proposed model is recommended because it considers the interaction between two different types of fillers and improves the prediction accuracy.

CONCLUSIONS

A micromechanics method, which was derived via Eshelby's equivalent inclusion method and Mori-Tanaka's back-stress analysis, was used to develop a three-phase model for polymer/clay/wood nanocomposites. We extended the method of Taya and Zhou to polymer/ellipsoidal filler/oblate platelet systems. The dominant structure of nanoclay in the nanocomposites was identified to be intercalation and partially exfoliation via XRD and TEM. Thus, intercalated clay particles along with the polymer in the galleries were treated as EOFs whose physical constants can be computed from the physical constants of the clay and the PLA matrix. The mathematical model involves five variables: a wood flour volume fraction f_1, a silicate layer volume fraction f_2, a silicate layer number n in an EOF, a wood flour aspect ratio α, and an EOF aspect ratio β.

The three-phase model recovers the limiting cases of two-phase models for polymer/ellipsoidal filler systems and for polymer/oblate platelet systems by setting either f_1 or f_2 zero. In the simplified polymer/ellipsoidal filler system, the model produced predictions fitting to the experimental results well in an aspect ratio (α) range of 2.4–5. In the simplified polymer/oblate platelet system, the predictions from our model related to the variation of the n value confirmed that intercalated clay structure is dominant in the nanocomposites, which is in good agreement with experimental observations. According to a maximum random packing theory and our model, the possible β range is from 44 to 75. Compared to our model, the Halpin-Tsai model tends to produce overestimated elastic modulus values when using same aspect ratios as those used in our model for the two simplified two-phase systems. In the three-phase nanocomposites, we achieved quantitative agreement between experimental data and our proposed three-phase model predictions for the following values of wood flour and EOF aspect ratios (α and β): $n = 2$, $\alpha = 3.7$, and $\beta = 75$. It is interesting to note that in our model predictions at a same β value, the increase rate of elastic modulus responding to the silicate layer volume fraction is larger at lower wood flour aspect ratio values than at larger α values.

ACKNOWLEDGMENTS

The authors gratefully acknowledge financial support via LEQSF grant RD-B-07 and NASA grant NNX08AP04A. This material was also based on work supported by the National Science Foundation, while DDK was working at the Foundation.

APPENDIX

$$C_{11}^{*} = \left(2S_{1111}^{1} + 2S_{1122}^{1} + S_{3311}^{1} + S_{3322}^{1}\right) + 2\left(\frac{\mu_1 - \mu_0}{\lambda_1 - \lambda_0}\right)\left(S_{1111}^{1} + S_{1122}^{1}\right) + \frac{2(\lambda_0 + \mu_0)}{(\lambda_1 - \lambda_0)} \quad \text{(A1.a)}$$

$$C_{12}^{*} = \left(2S_{1133}^{1} + S_{3333}^{1}\right) + 2\left(\frac{\mu_1 - \mu_0}{\lambda_1 - \lambda_0}\right)S_{1133}^{1} + \frac{\lambda_0}{\lambda_1 - \lambda_0} \quad \text{(A1.b)}$$

$$C_{21}^{*} = \left(2S_{1111}^{1} + 2S_{1122}^{1} + S_{3311}^{1} + S_{3322}^{1}\right) + 2\left(\frac{\mu_1 - \mu_0}{\lambda_1 - \lambda_0}\right)\left(S_{3311}^{1} + S_{3322}^{1}\right) + \frac{2\lambda_0}{(\lambda_1 - \lambda_0)} \quad \text{(A1.c)}$$

$$C_{22}^{*} = \left(2S_{1133}^{1} + S_{3333}^{1}\right) + 2\left(\frac{\mu_1 - \mu_0}{\lambda_1 - \lambda_0}\right)S_{3333}^{1} + \frac{\lambda_0 + 2\mu_0}{(\lambda_1 - \lambda_0)} \quad \text{(A1.d)}$$

$$D_1^* = 1 + \left(\frac{\mu_1 - \mu_0}{\lambda_1 - \lambda_0}\right) \tag{A1.e}$$

$$D_2^* = 1 + 2\left(\frac{\mu_1 - \mu_0}{\lambda_1 - \lambda_0}\right) \tag{A1.f}$$

The coefficients of C_{11}^{**}, C_{12}^{**}, C_{21}^{**}, C_{22}^{**}, D_1^{**}, and D_2^{**} for the inhomogeneity of type 2 (clay clusters) are of the same form as those for the type 1 but using the Eshelby tensors and Lamé constants (μ and λ) for type 2 instead of the corresponding ones for type 1.

$$\begin{aligned} A^* &= C_{11}^* C_{22}^* - C_{21}^* C_{12}^* \\ B_1^* &= 2\left(C_{12}^* - D_1^* C_{22}^*\right) \\ B_2^* &= D_2^* C_{12}^* - C_{22}^* \\ B_3^* &= 2\left(D_1^* C_{21}^* - C_{11}^*\right) \\ B_4^* &= C_{21}^* - D_2^* C_{11}^* \end{aligned} \tag{A2}$$

Type 2 inhomogeneities are identified by two asterisks superscripts.

$$\begin{aligned} H_{11}^* &= 2\left\{\frac{2v_0}{(1-2v_0)}\left(S_{1111}^1 + S_{1122}^1 + S_{3311}^1 - 1\right) + S_{1111}^1 + S_{1122}^1 - 1\right\} \\ H_{12}^* &= \frac{2v_0}{(1-2v_0)}\left(2S_{1133}^1 + S_{3333}^1 - 1\right) + 2S_{1133}^1 \\ H_{21}^* &= \frac{4v_0}{(1-2v_0)}\left(S_{1111}^1 + S_{1122}^1 + S_{3311}^1 - 1\right) + 4S_{3311}^1 \\ H_{22}^* &= \frac{2v_0}{(1-2v_0)}\left(2S_{1133}^1 + S_{3333}^1 - 1\right) + 2\left(S_{3333}^1 - 1\right) \end{aligned} \tag{A3}$$

The coefficients of H_{11}^{**}, H_{21}^{**}, H_{12}^{**}, and H_{22}^{**} can be obtained by substituting S_{ijkl}^1 with S_{ijkl}^2.

$$\begin{aligned} S &= Q_{11}Q_{22} - Q_{21}Q_{12} \\ S_1 &= Q_{12}R_2 - Q_{22}R_1 \\ S_2 &= Q_{21}R_1 - Q_{11}R_2 \end{aligned} \tag{A4}$$

$$\begin{aligned} Q_{11} &= \frac{2(1-f_1-f_2)}{(1-2v_0)} + f_1\left\{\frac{2}{(1-2v_0)} + \frac{\left(H_{11}^* B_1^* + H_{12}^* B_3^*\right)}{A^*}\right\} \\ &+ f_2\left\{\frac{2}{(1-2v_0)} + \frac{\left(H_{11}^{**} B_1^{**} + H_{12}^{**} B_3^{**}\right)}{A^{**}}\right\} \\ Q_{12} &= \frac{2v_0(1-f_1-f_2)}{(1-2v_0)} + f_1\left\{\frac{2v_0}{(1-2v_0)} + \frac{\left(H_{11}^* B_2^* + H_{12}^* B_4^*\right)}{A^*}\right\} \\ &+ f_2\left\{\frac{2v_0}{(1-2v_0)} + \frac{\left(H_{11}^{**} B_2^{**} + H_{12}^{**} B_4^{**}\right)}{A^{**}}\right\} \\ Q_{21} &= \frac{4v_0(1-f_1-f_2)}{(1-2v_0)} + f_1\left\{\frac{4v_0}{(1-2v_0)} + \frac{\left(H_{21}^* B_1^* + H_{22}^* B_3^*\right)}{A^*}\right\} \\ &+ f_2\left\{\frac{4v_0}{(1-2v_0)} + \frac{\left(H_{21}^{**} B_1^{**} + H_{22}^{**} B_3^{**}\right)}{A^{**}}\right\} \\ Q_{22} &= \frac{2(1-v_0)(1-f_1-f_2)}{(1-2v_0)} + f_1\left\{\frac{2(1-v_0)}{(1-2v_0)} + \frac{\left(H_{21}^* B_2^* + H_{22}^* B_4^*\right)}{A^*}\right\} \\ &+ f_2\left\{\frac{2(1-v_0)}{(1-2v_0)} + \frac{\left(H_{21}^{**} B_2^{**} + H_{22}^{**} B_4^{**}\right)}{A^{**}}\right\} \end{aligned} \tag{A5}$$

$$\begin{aligned} R_1 &= \frac{f_1}{A^*}\left\{H_{11}^*\left(B_2^* - v_0 B_1^*\right) + H_{12}^*\left(B_4^* - v_0 B_3^*\right)\right\} \\ &+ \frac{f_2}{A^{**}}\left\{H_{11}^{**}\left(B_2^{**} - v_0 B_1^{**}\right) + H_{12}^{**}\left(B_4^{**} - v_0 B_3^{**}\right)\right\} \\ R_2 &= \frac{f_1}{A^*}\left\{H_{21}^*\left(B_2^* - v_0 B_1^*\right) + H_{22}^*\left(B_4^* - v_0 B_3^*\right)\right\} \\ &+ \frac{f_2}{A^{**}}\left\{H_{21}^{**}\left(B_2^{**} - v_0 B_1^{**}\right) + H_{22}^{**}\left(B_4^{**} - v_0 B_3^{**}\right)\right\} \end{aligned} \tag{A6}$$

REFERENCES

1. LeBaron, P. C.; Wang, Z.; Pinnavaia, T. J. *Appl. Clay Sci.* **1999,** *15*, 11.
2. Thostenson, E. T.; Ren, Z. F.; Chou, T. W. *Compos. Sci. Technol.* **2001,** *61*, 1899.
3. Lloyd, D. J. *Int. Mater. Rev.* **1994,** *39*, 1.
4. Sanchez, C.; Ribot, F. *New J. Chem.* **1994,** *18*, 1007.
5. Messersmith, P. B.; Giannelis, E. P. *Chem. Mater.* **1994,** *6*, 1719.
6. Bledzki, A. K.; Gassan, J. *Prog. Polym. Sci.* **1999,** *24*, 221.
7. Stankovich, S.; Dikin, D. A.; Dommett, G. H. B.; Kohlhaas, K. M.; Zimney, E. J.; Stach, E. A.; Piner, R. D.; Nguyen, S. T.; Ruoff, R. S. *Nature* **2006,** *442*, 282.
8. Tucker C. L., III; Liang, E. *Compos. Sci. Technol.* **1999,** *59*, 655.
9. Luo, J. J.; Daniel, I. M. *Compos. Sci. Technol.* **2003,** *63*, 1607.
10. Taya, M.; Tsu-Wei, C. *Int. J. Solids Struct.* **1981,** *17*, 553.
11. Mori, T.; Tanaka, K. *Acta Metall.* **1973,** *21*, 571.
12. Eshelby, J. D. *Proc. Roy. Soc. A* **1957,** *241*, 376.
13. Meng, Q. Chemcial and Biomolecular Engineering; Tulane University: New Orleans, **2010; p 125.**
14. Mura, T. Micromechanics of Defects in Solids; Martinus Nijhoff Publishers: Dordercht, **1987.**
15. Meng, Q. K.; Hetzer, M.; De Kee, D. *J. Compos. Mater.* **2011,** *45*, 1145.
16. Huda, M. S.; Drzal, L. T.; Misra, M.; Mohanty, A. K. *J. Appl. Polym. Sci.* **2006,** *102*, 4856.
17. Ashton, J. E.; Halpin, J. C.; Petit, P. H. Primer on Composite Materials: Analysis; Conn: Techomic Pub. Co: Stamford, **1969.**
18. Fornes, T. D.; Paul, D. R. *Polymer* **2003,** *44*, 4993.
19. Sudduth, R. D. *Pigment Resin Technol.* **2008,** *37*, 362.
20. Sudduth, R. D. *Mater. Sci. Technol.* **2003,** *19*, 1181.
21. Sudduth, R. D., *J. Compos. Mater.* **2006,** *40*, 301.
22. Grande, C.; Torres, F. G. *Adv. Polym. Technol.* **2005,** *24*, 145.
23. Gacitua, W.; Bahr, D.; Wolcott, M., *Compos. Part A: Appl. Sci. Manuf.* **2010,** *41*, 1454.